Asymmetric cupula displacement due to endolymph vortex in the human semicircular canal

Goyens, J.; Pourquie, M. J.B.M.; Poelma, C.; Westerweel, J.

DOI
10.1007/s10237-019-01160-2

Publication date
2019

Document Version
Final published version

Published in
Biomechanics and Modeling in Mechanobiology

Citation (APA)
Goyens, J., Pourquie, M. J. B. M., Poelma, C., & Westerweel, J. (2019). Asymmetric cupula displacement due to endolymph vortex in the human semicircular canal. *Biomechanics and Modeling in Mechanobiology*, *18*(6), 1577-1590. https://doi.org/10.1007/s10237-019-01160-2

Biomechanics and Modeling in Mechanobiology
https://doi.org/10.1007/s10237-019-01160-2

ORIGINAL PAPER

Asymmetric cupula displacement due to endolymph vortex in the human semicircular canal

J. Goyens[1] · M. J. B. M. Pourquie[2] · C. Poelma[2] · J. Westerweel[2]

Received: 26 July 2018 / Accepted: 26 April 2019

Abstract
The vestibular system in the inner ear senses angular head manoeuvres by endolymph fluid which deforms a gelatinous sensory structure (the cupula). We constructed computer models that include both the endolymph flow (using CFD modelling), the cupula deformation (using FEM modelling), and the interaction between both (using fluid–structure interaction modelling). In the wide utricle, we observe an endolymph vortex. In the initial time steps, both the displacement of the cupula and its restorative forces are still small. As a result, the endolymph vortex causes the cupula to deform asymmetrically in an S-shape. The asymmetric deflection increases the cupula strain near the crista and, as a result, enhances the sensitivity of the vestibular system. Throughout the head manoeuvre, the maximal cupula strain is located at the centre of the crista. The hair cells at the crista centre supply irregularly spiking afferents, which are more sensitive than the afferents from the periphery. Hence, the location of the maximal strain at the crista may also increase the sensitivity of the semicircular canal, but this remains to be tested. The cupula overshoots its relaxed position in a simulation of the Dix-Hallpike head manoeuvre (3 s in total). A much faster head manoeuvre of 0.222 s showed to be too short to cause substantial cupula overshoot, because the cupula time scale of both models (estimated to be 3.3 s) is an order of magnitude larger than the duration of this manoeuvre.

Keywords Vestibular system · Fluid–structure interaction · Computational fluid dynamics · Time constant · Navier–Stokes equations · Balance · Finite element model

1 Introduction

The vestibular system in the inner ear senses linear and angular accelerations of the head. Therefore, it plays a crucial role in motor coordination and balance control, spatial awareness and navigation (Kandel et al. 1991; Latash 2008; Squire et al. 2013). The vestibular system is comprised of three interconnected semicircular tunnels in the temporal bone of the skull (the bony labyrinth, see Fig. 1). This bony labyrinth is filled with perilymph (a water-based fluid). Three interconnected ducts with membranous walls (the membranous labyrinth) float within the bony labyrinth. The ducts of the membranous labyrinth follow the semicircular shape of the bony labyrinth (see Fig. 1) and are also filled with a water-like fluid (called endolymph) (Kandel et al. 1991; Rabbitt et al. 2004; Latash 2008; Squire et al. 2013; Ekdale 2016). It is generally thought that the endolymph fluid lags behind due to its inertia when the head accelerates angularly. This causes flow of the (slower) fluid, relative to the (faster) membranous wall (Kandel et al. 1991; Muller and Verhagen 2002; Rabbitt et al. 2004, 2009; Angelaki and Cullen 2008; Latash 2008; Ekdale 2016; Grohé et al. 2016; Djukic and Filipovic 2017). The relative endolymph flow deflects sensory hairs, resulting in a neural signal to the brain. The sensory hairs originate from sensory epithelia on crest-like ridges (crista) in the labyrinth walls. The sensory hair bundles are embedded in gelatinous structures, the cupulae, which are located in widened parts of the semicircular canals (called ampullae), at each end of the semicircular ducts (see Fig. 1). The cupulae are attached to the ampulla walls along their entire perimeter, like a diaphragm

Electronic supplementary material The online version of this article (https://doi.org/10.1007/s10237-019-01160-2) contains supplementary material, which is available to authorized users.

✉ J. Goyens
jana.goyens@uantwerpen.be

[1] Laboratory of Functional Morphology, University of Antwerp, Universiteitsplein 1, 2610 Wilrijk, Belgium

[2] Laboratory for Aero and Hydrodynamics, Delft University of Technology, Mekelweg 2, 2628 LD Delft, The Netherlands

Published online: 08 May 2019

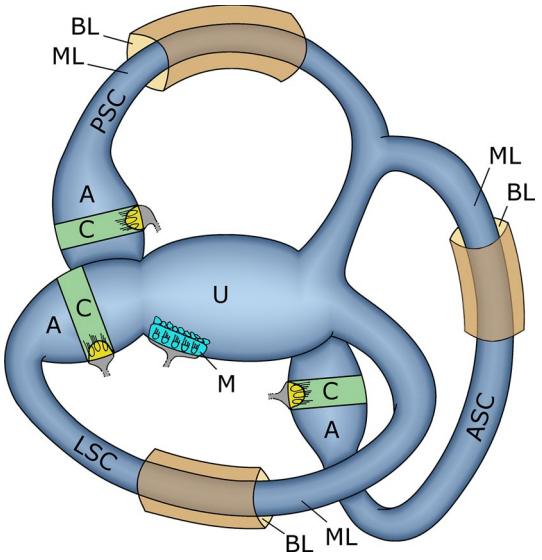

Fig. 1 Schematic drawing of the vestibular system. Sizes and colours for illustration purposes only. The membranous labyrinth (ML, blue) consists of three semicircular ducts (the lateral semicircular canal, LSC; the posterior semicircular canal, PSC; the anterior semicircular canal, ASC). They run entirely within the bony labyrinth (BL, brown), which is only depicted at three places. Each duct ends in an ampulla (A), in which a cupula (light green, C) with crista (yellow) is located. All ampullas end in the utricle (U), which houses a macula (turquoise, M)

(McLaren and Hillman 1979; Rabbitt et al. 2004, 2009; Cullen 2012; Ekdale 2016). The three ampullas open in the utricle, a single larger chamber that hosts linear accelerometers (maculas with otolith crystals) (Kandel et al. 1991; Latash 2008; Squire et al. 2013).

The deflection of the cupula—and, therefore, also the neural signal—in response to head rotation is determined by the fluid dynamics of the endolymph. Numerous authors have developed mathematical descriptions of the macromechanical fluid properties of the vestibular system using differential equations (overdamped, second order). Starting with Lorente de Nó (1927), the fluid dynamics were investigated for a single toroidal duct with uniform cross section without the cupula. Later, the cupula was included (Steinhausen 1933; Van Buskirk et al. 1976), and the semicircular duct was modelled with a non-uniform cross section (Oman et al. 1987). Other authors succeeded in modelling interconnected ducts (Muller and Verhagen 1988), obtaining analytical solutions (Muller and Verhagen 2002; Obrist 2008) and included inertial-viscoelastic behaviour of the cupula (Rabbitt et al. 1995; Rabbitt 1999). Important information on factors influencing the sensitivity, response time, time constants, and endolymph flow was gained from these analytical models with a (relatively) simple anatomy.

The development of numerical simulation software (and affordable fast computers) subsequently enabled much more complicated and realistic geometries of semicircular ducts and cupulae to be investigated. These models were mainly developed to gain a better understanding of vestibular pathologies and clinical practices (e.g. Kassemi et al. 2005; Boselli et al. 2014; Grieser et al. 2016; Djukic and Filipovic 2017). For example, the computational model by Boselli et al. (2014) of the fluid-particle dynamics of a semicircular canal with benign paroxysmal positional vertigo (BPPV) showed the particle displacement within the canal after a provocative head manoeuvre. The model output may explain BPPV fatigue during a consecutive head manoeuvre. The 2D simulations of endolymph and cupula by Kassemi et al. (2005) helped us to understand the caloric irrigation test, and the computer model of the endolymph and the wall of the membranous labyrinth by Grieser et al. (2016) showed how pathogenic wall deformations due to sound stimuli cause endolymph flow and cupula oscillations during the so-called Tullio phenomenon. Similar to most analytical models, the cupula is only implicitly modelled in many numerical simulation models, for example, by introducing a pressure difference in response to the volume of displaced endolymph (Obrist 2011; Boselli et al. 2013, 2014, Grieser et al. 2013, 2016). In these models, endolymph flow through the ampulla remains possible. This is an unnatural situation, however, because in reality, the cupula fills the entire cross section of the endolymph such that endolymph flow is blocked (McLaren and Hillman 1979; Yamauchi et al. 2002; Rabbitt et al. 2004, 2009). Recently, some authors have resolved this issue by combining 3D fluid simulations of the endolymph with a 3D finite element model of the cupula in a single model (Djukic and Filipovic 2017; Santos et al. 2017a). Kassemi et al. (2005) and Wu et al. (2011) previously did the same in 2D. Such fluid–structure interaction (FSI) models couple a fluid simulation and a structural simulation of the endolymph and the cupula, respectively. These models take into account the forces that are exerted by the fluid on the cupula, as well as the incremental displacement of the cupula that displaces fluid. However, the communication between the fluid and the structural parts of the FSI model is notoriously a technical challenge, which is further complicated by the very low elasticity of the cupula [which has a Young's modulus of only approximately 5 Pa (Selva et al. 2009; Wu et al. 2011; Santos et al. 2017a)].

1.1 Aims of the present study

The current study rigorously investigates this new 3D fluid–structure interaction modelling of the vestibular system. It includes the endolymph, modelled by computational fluid dynamics (CFD); the cupula, modelled by finite element modelling (FEM) and the interaction between both. This will give us the possibility to investigate, in detail, the cupula displacement during head manoeuvres, and in

Table 1 Overview of simulation models

Model	Geometry	Simulation type	Velocity profile
T	Torus (see Fig. 2a)	CFD only	Ramp, alarm turn (see Fig. 3b)
H	Human (see Fig. 2b)	CFD only	Ramp, alarm turn (see Fig. 3b)
O	Human (open ampulla)	CFD only	Ramp, alarm turn (see Fig. 3b)
F	Human (see Fig. 2b)	FSI	Ramp, alarm turn (see Fig. 3b)
S	Human (see Fig. 2b)	FSI	Smooth, alarm turn (see Fig. 3a)
DH	Human (see Fig. 2b)	FSI	Smooth, Dix-Hallpike (see Fig. 3c)

CFD stands for computational fluid dynamics, *FSI* stands for fluid–structure interaction model

particular, the effect of the endolymph vortex in the utricle which was first described by Boselli et al. (2013). While the existing 3D FSI models in the literature have a very simplified, toroidal geometry (Djukic and Filipovic 2017; Santos et al. 2017b), we constructed a realistic geometry of the human lateral semicircular canal and utricle, based on the anatomical literature. A further novel aspect of the current study is the analysis of the relative magnitude of the terms in the Navier–Stokes (NS) equations. The NS equations determine the movement of fluid; hence, calculating the terms of these equations enables us to obtain an in-depth evaluation of the relative importance of viscosity, the pressure gradient, inertia, and advection within the vestibular system, supplemented with fictitious forces (Coriolis, centrifugal, and Euler) in the case of a relative frame of reference (Batchelor 2007).

1.2 Organization of this paper

We built a series of models of increasing complexity. Comparison of models with a torus geometry (model T) and a human geometry (model H) revealed the effect of the widened utricle and ampulla on the endolymph dynamics. Comparison of model H and a model with an open ampulla (i.e. without cupula, model O) showed the effect of continuous endolymph flow through the ampulla. Next, we added a deformable cupula (model F) and compared this with model H, which has an extremely stiff cupula. On models T, H, O, and F, we imposed a head manoeuvre with a ramp velocity profile, which facilitates interpretation because of the constant acceleration during spinup and spindown and the clear onset and end of both. Finally, we simulated two models with a smooth and realistic head manoeuvre. In the first (model S), we imposed a natural, fast head rotation; while in the second (model DH), we imposed a clinical, slow, Dix-Hallpike manoeuvre.

In the results section, we first describe the endolymph flow and pressure (Sect. 3.1). We then take model S as a reference and compare its outcome to the other models. Likewise, we report the cupula deformation and strain in model S in Sect. 3.2. Results Sect. 3.3 is devoted to the Dix-Hallpike manoeuvre and how this compares to model S and the model by Boselli et al. (2013). Finally, in Sect. 3.4, we describe the NS terms for models T, H, O, F, and S (see Table 1).

2 Materials and methods

2.1 3D morphology and mesh

In the first model (model T, see Table 1), we used a torus as a very simplified geometry of a horizontal semicircular duct. This torus was constructed in Ansys DesignModeler (version 17.2, Pittsburgh, USA) and had a major radius of 3.2×10^{-3} m and a minor radius of 5.75×10^{-4} m (see Fig. 2a). These dimensions are based on the ampullar dimensions in Obrist (2011). A disc-shaped cupula was included with a thickness of 4.03×10^{-4} m [cf. (Kassemi et al. 2005; Selva et al. 2009)]. In Ansys Meshing (version 17.2, Pittsburgh, USA), we converted the torus model into a tetrahedral mesh with a maximal edge length of 5×10^{-5} m, which contained 1454 k elements.

For the other models (models H, O, F, S, and DH; see Table 1), we used the geometry of the human lateral semicircular canal, based on the measurements of the membranous labyrinth by Curthoys and Oman (1987) (see Fig. 2b). In Ansys DesignModeler, we converted the 2D measurements (heights and widths of cross sections of the membranous labyrinth) into a smooth 3D geometry using sweeps between ellipses. In models H, F, S, and DH, we inserted a cupula with a uniform thickness of 4.03×10^{-4} m [cf. (Kassemi et al. 2005; Selva et al. 2009)] and subtracted a crista with a height of 5×10^{-7} m from the geometry in the ampulla (Curthoys and Oman 1987). In model O, the ampulla remained open (i.e. there is no cupula, and as a result there is a continuous loop of endolymph, see Fig. S2A, B). We created a tetrahedral mesh in Ansys Meshing with a maximal edge length of 5×10^{-5} m in the fluid (endolymph) part and 6.88×10^{-5} m in the cupula. We refined the mesh in the narrow part of the semicircular duct. This resulted in 13 k elements in the cupula and 946 k elements in the endolymph. The composite element quality metric (provided by Ansys Meshing) was 0.82 ± 0.13 and 0.84 ± 0.10 in the cupula and the endolymph, respectively. The element aspect

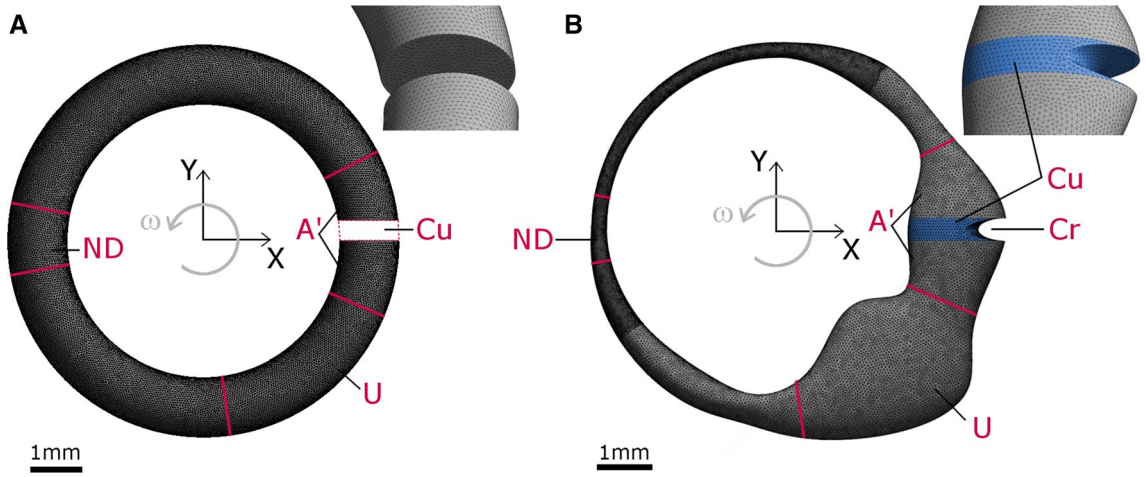

Fig. 2 3D geometry of the torus (**a**) and human lateral semicircular canal (**b**). The borders of the ampulla (A′), utricle (U) and narrow duct (ND) zones used in the results section are shown by red lines. 'Cr' denotes the crista. The cupula (Cu) walls are depicted with a red dashed line in A. The rotation direction of the angular velocity (ω) is shown in grey. The insets show a detail of the mesh in the ampulla in an oblique view

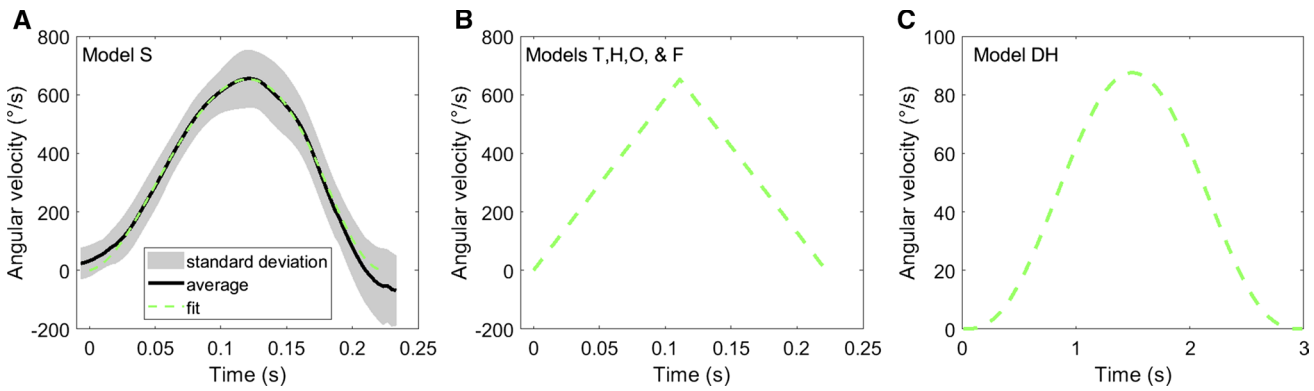

Fig. 3 Prescribed angular velocity of the relative reference frame. **a** Average (±standard deviation) of measured alarm turn head manoeuvre and polynomial fit. **b** Ramp profile of angular velocity. **c** Dix-Hallpike head manoeuvre, calculated with the polynomial described by Obrist et al. (2010). The scale of the *Y*-axis differs between subplots

ratio was 2.1 ± 0.2 and 1.8 ± 0.4 in the cupula and the endolymph, respectively. The number of elements used in our model reflects a compromise between computation time and accuracy. A simulation of model S with twice the number of elements yielded almost identical results, showing that the chosen number of elements is sufficient (percentage of pressure difference over cupula between finer and coarser grid: 0.25 ± 0.49%; of volume swept by cupula: -0.54 ± 0.60%; of Navier–Stokes terms: -0.014 ± 0.45%).

2.2 Head manoeuvre

To simulate a realistic head manoeuvre, we measured the head rotation of six healthy adults (two women and four men) who were asked to suddenly look sidewards (as in the case of hearing an unexpected noise behind their shoulder). We will call this head manoeuvre the "alarm turn manoeuvre". Top view high-speed video recordings were made in spring 2016 in the context of research performed in the M^2OCEAN laboratory regarding the evaluation of postural control and locomotion (approved by the local ethics committee, registration number B300201316320). These recordings were used to deduce head rotations. The test subjects turned their head in 0.222 s ± 0.064 s over 80.0° ± 11.5° in the XY-plane (the plane of the horizontal semicircular canal) (see Fig. 3a). We fitted a polynomial through the average angular velocity (ω) in order to impose it on the computational fluid dynamics and finite element analysis models.

In models T, H, O, and F, we used a simplified version of this velocity profile, in which the angular velocity first increased linearly to the maximal velocity of the polynomial ($\omega = 11.4$ rad/s, "ramp up") over 0.111 s and subsequently

linearly decreased back to 0 rad/s in 0.111 s ("ramp down") (see Fig. 3b).

To enable us to make a comparison with the numerical simulation model of the human lateral semicircular canal by Boselli et al. (2013), we additionally imposed the "Dix-Hallpike" head manoeuvre on an FSI model (model DH) that was, for the rest, identical to model S. This is a clinical head manoeuvre that is often used in experiments and simulations, in which the head is rotated in 3 s over 120° in the plane of the canal (see Fig. 3c). Hence, it is a much slower manoeuvre than the fast alarm turn that we used in the other simulations.

2.3 Computational fluid dynamics of the endolymph

We modelled the endolymph flow in Ansys Fluent (version 18.0, Pittsburgh, USA). Due to the low Reynolds number, we used a laminar viscous model. We used a pressure-based solver with second-order spatial discretization and first-order implicit time integration for the temporal discretization (Ansys Fluent Theory Guide section 21.3.2). The pressure–velocity coupling scheme was "simple". The material properties of the endolymph resemble those of water, so we used a density of 998.2 kg/m^3 and a viscosity of 0.001 Pa s (Steer et al. 1967; Rabbitt et al. 2004; Kassemi et al. 2005; Boselli et al. 2013; Grieser et al. 2013). We allowed density fluctuations in the FSI simulations ("compressible liquid" setting in models F, S, and DH; Ansys Fluent User Manual section 7.3.4). This avoided errors in cases of slight fluid volume changes due to cupula displacements; this was necessary because the model contains no inlets or outlets. The fluid density at the end of the time step proved to be almost constant, with hardly any variation in space or time ($<$ 1e−5). The membranous walls were modelled as 'no slip' walls.

We inserted the head manoeuvre with a user-defined function for frame motion into Fluent in models F, S, and DH. The "Define Zone Motion" macro in Fluent allows for rotation of the reference frame and causes the walls of the geometry to move together with this reference frame. When we refer to the "absolute reference frame", we refer to the earthbound frame. In this reference frame, the walls are rotating. When we refer to the "relative reference frame", we refer to the reference frame that is moving together with the rotating walls. Hence, in the latter case, the walls stand still and fluid flow is defined as movement relative to these walls. In a rotating and accelerating reference frame, we needed to include additional fictitious terms in the NS equation, the so-called Coriolis terms, centrifugal terms and Euler terms (Batchelor 2007, see also Sect. 2.6). The origin of both reference frames is located in the centre of the semicircular duct (see Fig. 2). Both the simulation with the smooth acceleration profile (model S) and those with the ramp velocity profile (models T, H, O and F) were further run after the end of the head manoeuvre (from 0.222 to 0.3 s) at an angular velocity of zero rad/s in order to allow the fluid flow and cupula deformations to come to rest. We always used a time step size of 0.001 s and 100 iterations per time step, which typically resulted in residuals for continuity and x-, y-, and z-velocity of 1e−5, 1e−7, 1e−7, and 1e−8, respectively.

2.4 Finite element analysis of the cupula

The finite element model of the cupula was constructed in Ansys transient structural (version 18.0, Pittsburgh, USA) for models F, S, and DH. (In models T and H, the cupula walls are modelled as rigid walls; model O does not have a cupula.) Consistent with values cited in the literature, we used a Young's modulus of 5.4 Pa and a Poisson ratio of 0.3 (Kassemi et al. 2005; Selva et al. 2009; Wu et al. 2011; Santos et al. 2017a). A fixed support boundary condition was used for the cupula elements that touched the walls of the membranous labyrinth and crista. The movement of this cupula edge as a result of the head manoeuvre was included as a "rotational velocity" boundary condition.

2.5 Fluid–structure interaction of endolymph and cupula

The fluid–structure interaction of the endolymph (fluid) and the (solid) cupula in the F, S, and DH models was performed using the system coupling module of ANSYS Workbench (version 18.0, Pittsburgh, USA). We transferred the force, which was calculated for every fluid element by Fluent, to the neighbouring cupula element. Next, we calculated the cupula deformation caused by this force in transient Structural, and we moved the neighbouring fluid elements accordingly. This cycle was repeated seven times for each time step of 0.001 s. (This number of repetitions was determined after a manual optimization based on the average pressure difference over the cupula). Following the FSI manual by Ansys, we enabled dynamic remeshing in Fluent, which changes the fluid mesh when the fluid elements have to move and reshape because of cupula deformations. Further, we applied a coefficient-based solution stabilization factor of 1.5, which was necessary because FSI simulations that include structural materials with a low Young's modulus are often unstable. A slight overestimation of the structural deformation would lead to oscillating fluid pressures and structural deformations, causing the model to diverge. Solution stabilization enables a slower increase or decrease in the fluid pressure during the iteration process, causing the simulation to converge gradually towards the equilibrium

between the fluid force and the structural deformation without oscillating around it. This does not influence the final outcome of the Fluent calculations (see Ansys Fluent User Manual section 10.6.8.7) (Berg 2011).

2.6 Time constants

Two time scales describe the frequency range of head rotations in which the volume displacement of the cupula is proportional to the angular velocity of the head (Rabbitt et al. 2004). We calculated the short time scale (the viscous time constant) as the time lag between head acceleration and endolymph velocity in models S and DH (Grieser et al. 2013). When a head manoeuvre is faster than this constant, the vestibular response is attenuated by the inertia of the endolymph in the narrow duct (Rabbitt et al. 2004). Additionally, the long time scale (the cupula time constant) was calculated in MATLAB as the relaxation time of the volume swept by the cupula in models S and DH (Njeugna et al. 1992; Obrist et al. 2010; Boselli et al. 2013; Grieser et al. 2016), i.e. the time lag between the end of the head movement and the instant the volume swept by the cupula reaches zero. The cupula did not reach its relaxed shape by the end of the simulations, but the volume swept by the cupula did decrease towards the end (period indicated with a yellow box in Fig. 5b). Hence, we estimated the long time scale using a linear regression of the volume swept in this period. As previous simulation models suggest that the cupula relaxation may slow down over time (Obrist 2011; Boselli et al. 2013), our approach may lead to an underestimation of the long time scale. The vestibular response to rotations that are slower than the long time scale that is attenuated by the stiffness of the cupula (Rabbitt et al. 2004).

2.7 Navier–Stokes terms

To evaluate the relative importance of viscosity, inertia, advection, and pressure in our models, we calculated the Navier–Stokes terms for all fluid elements with a user-defined function in Fluent. We used the "Execute At End" macro for this purpose, which was run once at the end of each time step. Median values were calculated for the zones indicated in Fig. 2.

In the absolute (earthbound) reference frame, the Navier–Stokes equations for an incompressible fluid without external forces are (Batchelor 2007):

$$\rho\frac{\partial \boldsymbol{u}}{\partial t} + \rho(\boldsymbol{u}\cdot\nabla)\boldsymbol{u} = -\nabla P + \mu\nabla^2\boldsymbol{u} \tag{1}$$

with $\boldsymbol{u}$ the fluid velocity vector, P the static pressure, ρ the fluid density (998.2 kg/m^3), and μ the dynamic viscosity (0.001 Pa s).

We also calculated the Navier–Stokes terms in the relative (head-bound) reference frame. In this case, we added the Coriolis, centrifugal, and Euler terms to the Navier–Stokes equations (Batchelor 2007):

$$\rho\frac{\partial \boldsymbol{v}}{\partial t} + \rho(\boldsymbol{v}\cdot\nabla)\boldsymbol{v} = -\nabla P + \mu\nabla^2\boldsymbol{v} - 2\boldsymbol{\Omega}\times\boldsymbol{v} - \boldsymbol{\Omega}\times(\boldsymbol{\Omega}\times\boldsymbol{r}) - \frac{\partial \boldsymbol{\Omega}}{\partial t}\times\boldsymbol{r} \tag{2}$$

with $\boldsymbol{v}$ the fluid velocity vector relative to the velocity of the moving reference frame, $\Omega = (0, 0, \omega)$ the angular velocity vector of the moving reference frame, and $\boldsymbol{r}$ the radial coordinate of the endolymph element.

3 Results

3.1 Endolymph flow and pressure

Model S is (together with model DH) the most realistic model, including a deformable cupula in a human-shaped SCC that is smoothly rotated in anticlockwise direction. While the walls accelerate angularly, the fluid near the walls is dragged along because of the non-slip condition. As a result, the absolute fluid velocity is higher at the outer border than at the inner border (see Fig. 4a, c), and the relative fluid velocity is zero at both borders (see Fig. 4b, d). The relative velocity inside the lumen of the SCC stays an order of magnitude lower than the velocity of the walls (maximum velocity of, respectively, 3.7×10^{-3} m/s and 3.4×10^{-2} m/s). Nevertheless, it is instructive to investigate the velocity in the relative frame of reference because this is the reference frame of the cupula.

The relative velocity is elevated in both the narrow duct and the utricle (see Fig. 4b). The elevated relative velocity in the narrow duct is caused by the deflecting cupula, which allows relative fluid flow towards the concave side of the cupula during acceleration (i.e. in clockwise direction; from low towards high pressure; see Fig. 4b). In the model with a rigid cupula (model H), the cupula does not deform and hence, hardly any flow velocity exists in the narrow duct relative to the walls. The elevated relative velocity in the utricle is present as a vortex that flows in clockwise direction during acceleration and suddenly changes direction when the walls start decelerating (see Fig. 4e, f). This vortex results from the widened shape of the utricle. Hence, it does not appear in the model of a torus (model T, see Fig. 4g), while it is present in all models with a human geometry (models H, F, and S). The vortex still develops in a simulation in which the endolymph is modelled as an inviscid fluid (see Fig. S2). It has to be noted that this is a purely hypothetical situation, in which the relative flow velocities are different from those in reality.

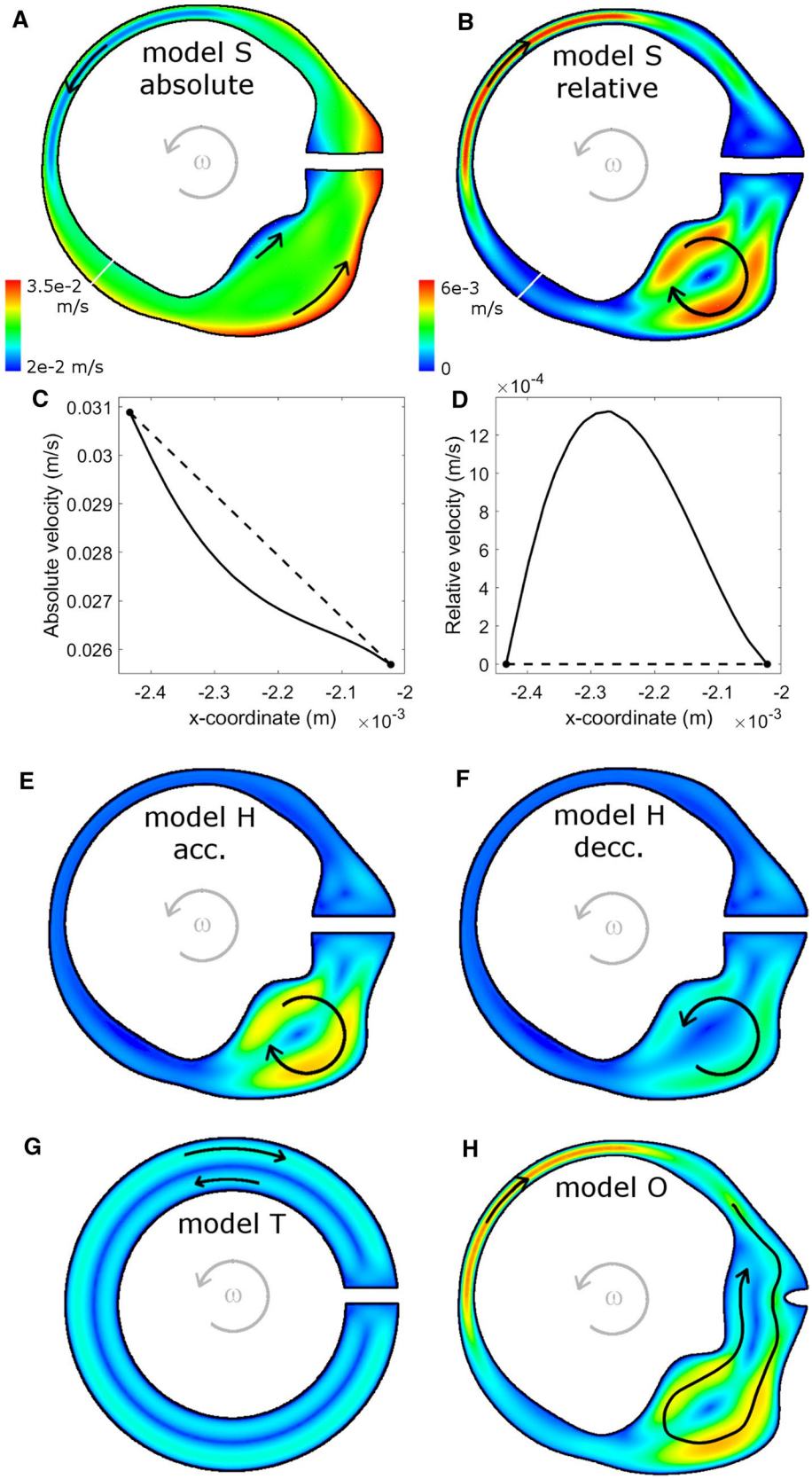

Fig. 4 Endolymph velocity in the XY-plane at $t = 0.08$ s (except for F:$t = 0.16$ s). **a** and **c**: absolute velocity. **b** and **d**–**h**: relative velocity. The colour scale is the same for all relative velocity plots. Grey arrows show the rotation direction of the head manoeuvre; black arrows schematically show the endolymph flow direction and have an arbitrary size. It is important to note that the relative flow velocities are very low, hence, any given fluid particle does not flow entirely from the utricle into the ampulla or vice versa. **c** and **d** show the velocity magnitude of the cross sections that are indicated with white lines in **a** and **b**

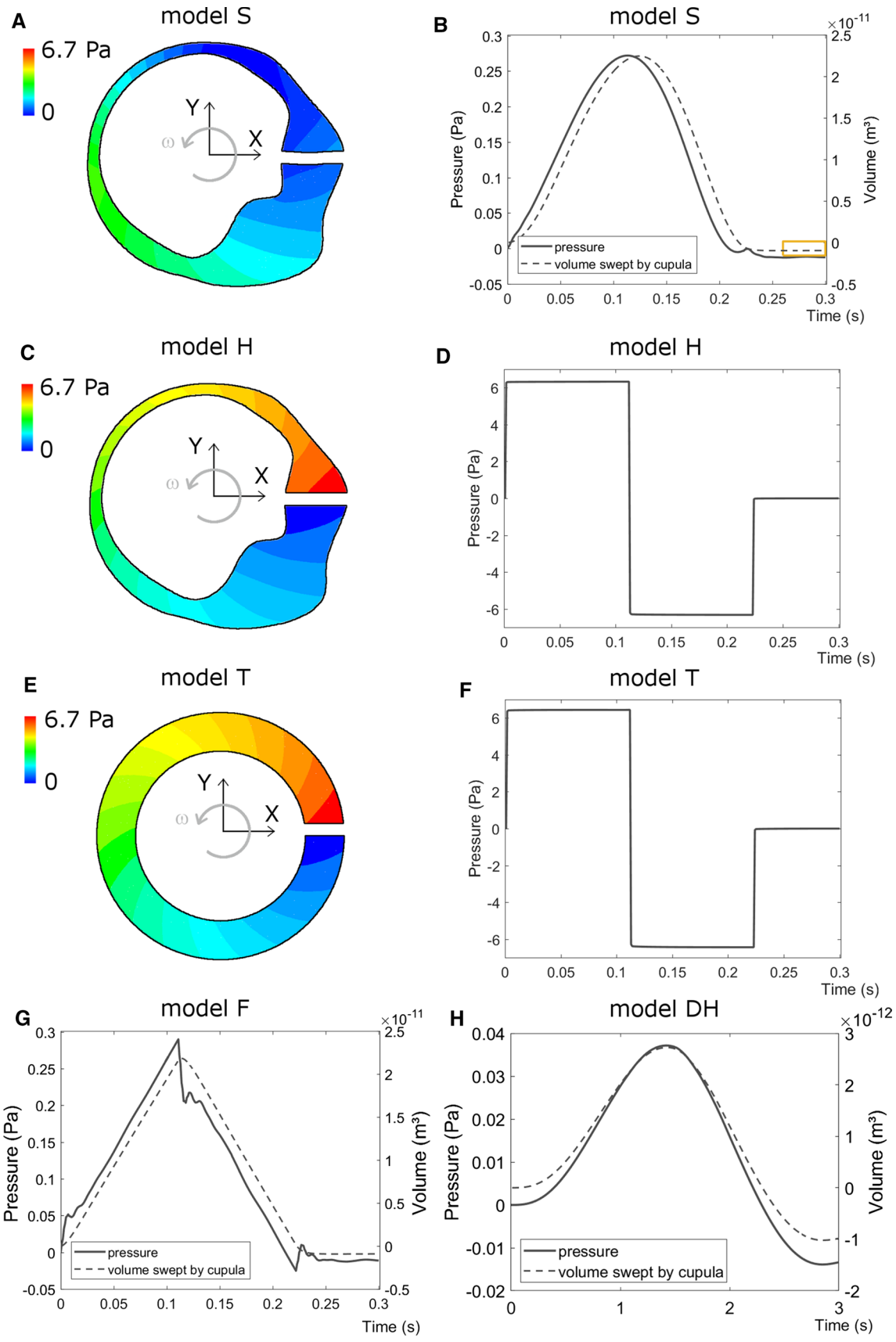
A
model S
6.7 Pa
0
Y
X
ω
B
model S
×10^-11
Pressure (Pa)
Volume (m³)
pressure
volume swept by cupula
Time (s)
C
model H
6.7 Pa
0
Y
X
ω
D
model H
Pressure (Pa)
Time (s)
E
model T
6.7 Pa
0
Y
X
ω
F
model T
Pressure (Pa)
Time (s)
G
model F
×10^-11
Pressure (Pa)
Volume (m³)
pressure
volume swept by cupula
Time (s)
H
model DH
×10^-12
Pressure (Pa)
Volume (m³)
pressure
volume swept by cupula
Time (s)

◂**Fig. 5** Endolymph pressure and cupula volume displacement. **a**, **c** and **e**: Contours plots of the endolymph pressure in the XY-plane at $t = 0.08$ s. Grey arrows show the rotation direction of the head manoeuvre. **b**, **d**, **f**, **g** and **h**: Time profile of the pressure difference over the cupula (averaged across its surface) and of the volume swept by the cupula

The angular acceleration of the walls causes an endolymph pressure difference over the cupula (see Fig. 5a, b). The SCC is accelerated in anticlockwise direction, which causes the fluid pressure to increase at the 'upstream' ampulla halve (positive *Y*-coordinates) and to decrease at the 'downstream' ampulla halve (negative *Y*-coordinates) due to the inertia of the fluid. This is more clearly visible in model H with a rigid cupula (see Fig. 5c), because the deforming cupula of model S also influences the pressure distribution which complicates the interpretation (see Fig. 5a). This is probably the effect of the fluid flow, relative to the rotating walls, which is possible when the cupula is deformable. The profile of the average pressure difference over the cupula is smooth in model S because of its smooth acceleration profile and its deformable cupula (see Fig. 5b). In the models with a ramp velocity profile and a rigid cupula (models T and H), the step-like acceleration pattern of the SCC is reflected in the pressure velocity profile (rather than having a smooth profile, see Fig. 5d, f). For example, in model T, the average pressure difference over the cupula is 6.44 Pa during the entire acceleration phase and − 6.44 Pa during the entire deceleration phase. This equals the theoretically predicted average pressure difference of 6.44 Pa based on $P = F/A = (m \times a)/A$ (with m the endolymph mass, a the linear acceleration of the walls and A the cross-sectional area of the cupula). In model F, a deformable cupula is introduced and, as a result, the pressure difference over the cupula rises gradually instead of immediately attaining a constant value while the walls are accelerating (see Fig. 5g). The average pressure difference also remains much lower in models F and S with deformable cupulas than in model H with a rigid cupula (see Fig. 5b, d, g). Because of the abrupt changes in velocity that are imposed on the SCC in model F, numeric artefacts arise in the pressure difference over the cupula at the onset and end of acceleration and deceleration (see Fig. 5g). This is the downside of the simple ramp velocity profile, which we used in model T and H for ease of interpretation.

3.2 Cupula deformation and strain

The finite element analysis part of the fluid–structure interaction model shows how the cupula deforms during the head manoeuvre. Initially, the cupula deforms asymmetrically: at the outer side of the ampulla (near the crista), it bulges in clockwise direction; while at the inner side of the ampulla, it bulges in anticlockwise direction (see Fig. 6a, b, supplementary movie S12). The velocity profile of the cupula resembles the fluid velocity profile at the same location in the model with an open ampulla in these initial time steps (model O; see Fig. 6b), but the amplitude of the cupula velocity is lower (47.6% of the maximal fluid velocity in model O). Gradually, the deformation at the outside increases at the expense of the bulge in anticlockwise direction until the latter disappears at 0.05 s. The cupula shape remains more or less symmetrical until 0.034 s before the end of the head manoeuvre, when the cupula starts bulging in anticlockwise direction near the crista (see Fig. 6a). This gradually increases and eventually becomes larger than the bulge in clockwise direction at the inner side of the ampulla. After the end of the head manoeuvre, this overshoot in anticlockwise direction fades away in 3.33 s; which defines the long time scale of the system.

While the cupula displacement increases during head acceleration, the maximal strain at the crista surface rises (see Fig. 6c). During deceleration, the cupula displacement and strain decrease, until the cupula overshoot leads to a small increase in cupula strain at the end of the head manoeuvre (see Fig. 6c). During the entire head manoeuvre (also when the cupula deforms asymmetrically), the elastic equivalent strain (Von-Mises strain) is the highest at the centre of the crista and decreases towards the periphery (see Fig. 6e). In a hypothetical simulation of a cupula without crista (i.e. an oval, disc-shaped cupula), on the other hand, the strain at the cupula attachment surface is the highest at the edges and minimal in the centre (see Fig. 6f).

3.3 Dix-Hallpike manoeuvre

Due to the lower head acceleration (angular head velocity up to, respectively, 87°/s and 653°/s), the cupula displacement is smaller during the Dix-Hallpike manoeuvre than during the alarm turn manoeuvre (volume displacement up to, respectively, 2.7×10^{-12} m^3 and 2.2×10^{-11} m^3, see Fig. 5b, h). While the cupula hardly overshoots its relaxed position in the alarm turn head manoeuvre, there is a pronounced cupula overshoot in the slower Dix-Hallpike manoeuvre. The overshoot in the Dix-Hallpike simulation is larger than found in the numerical simulation model with an implicitly modelled cupula by Boselli et al. (2013). Further, the general shape of the volume displacement profile is similar, the maximal values lie close together (respectively, 2.7e−12 m^3 and 2.4e−12 m^3) and the overshoot starts at approximately the same time (at 2.3 s and 2.5 s, respectively).

3.4 Navier–Stokes terms

In the relative reference frame (which is perhaps the most relevant reference frame because the cupula is attached to

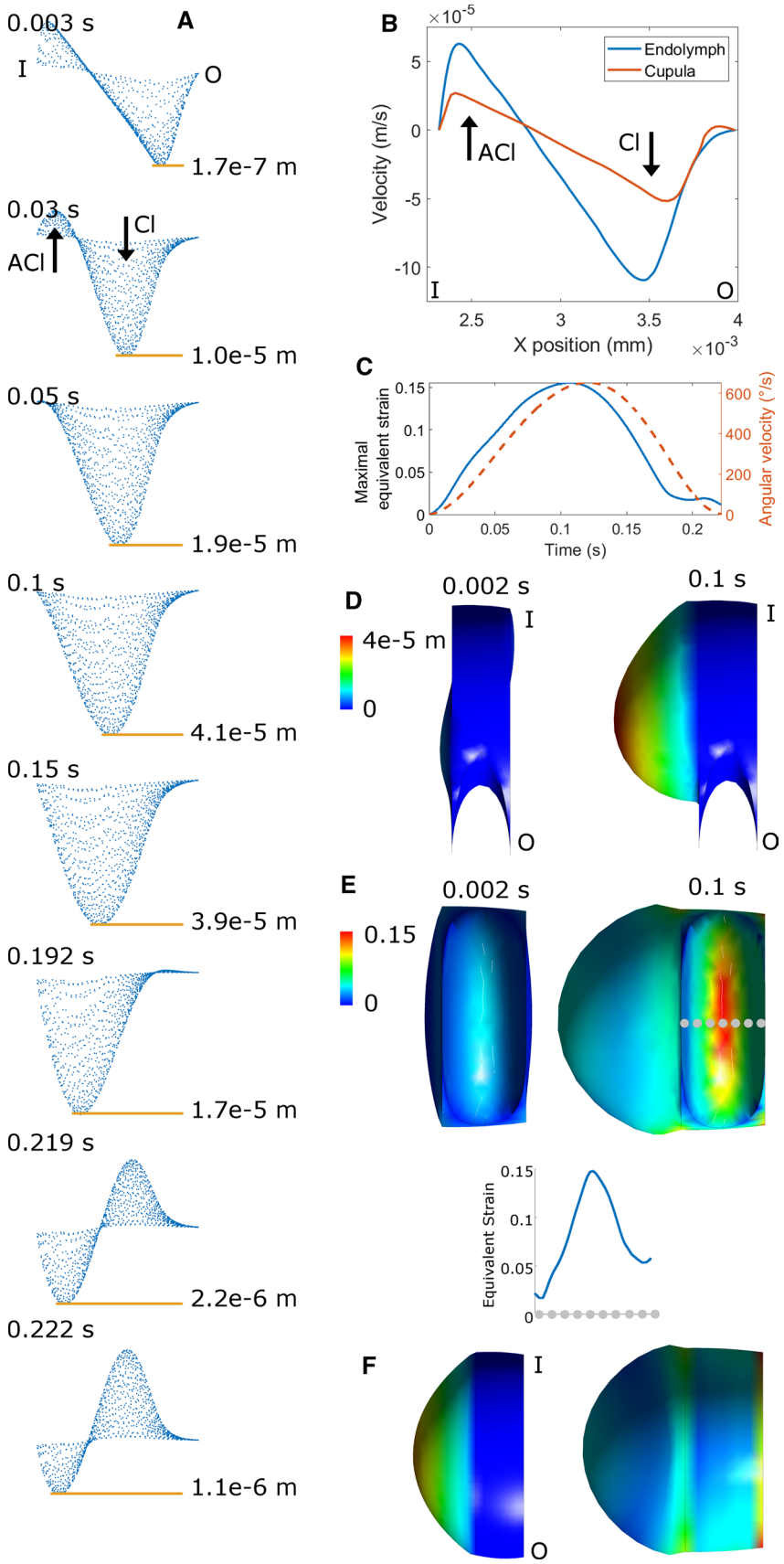

Fig. 6 Cupula displacement and strain in model S. **a** Cupula displacement through time. The total displacement is scaled to the same magnitude for all time steps. **b** Velocity of the cupula interaction surface in model S and endolymph velocity at the same location in model O at $t = 0.002$ s. **c** Maximal cupula strain at the crista surface (blue solid line) and the angular velocity of the head manoeuvre (orange dashed line) through time. **d** XY-view (top view) of the cupula displacement. **e** YZ-view (view from the crista into the cupula) of the cupula strain. The line graph shows the strain of the crista surface cross section shown by the dotted line. **f** Displacement in XY-view (left) and strain in YZ-view (right) of a cupula without crista (i.e. an oval shaped disc) under a static pressure of 0.26 Pa. The colour scales are the same as in **c** and **d**. The cupula displacement in **d**–**f** is enlarged by a factor of 15 for visualization purposes. *Cl* Clockwise direction, *ACl* anticlockwise direction, *I* inner side of the cupula, *O* outer side of the cupula (where the crista is located)

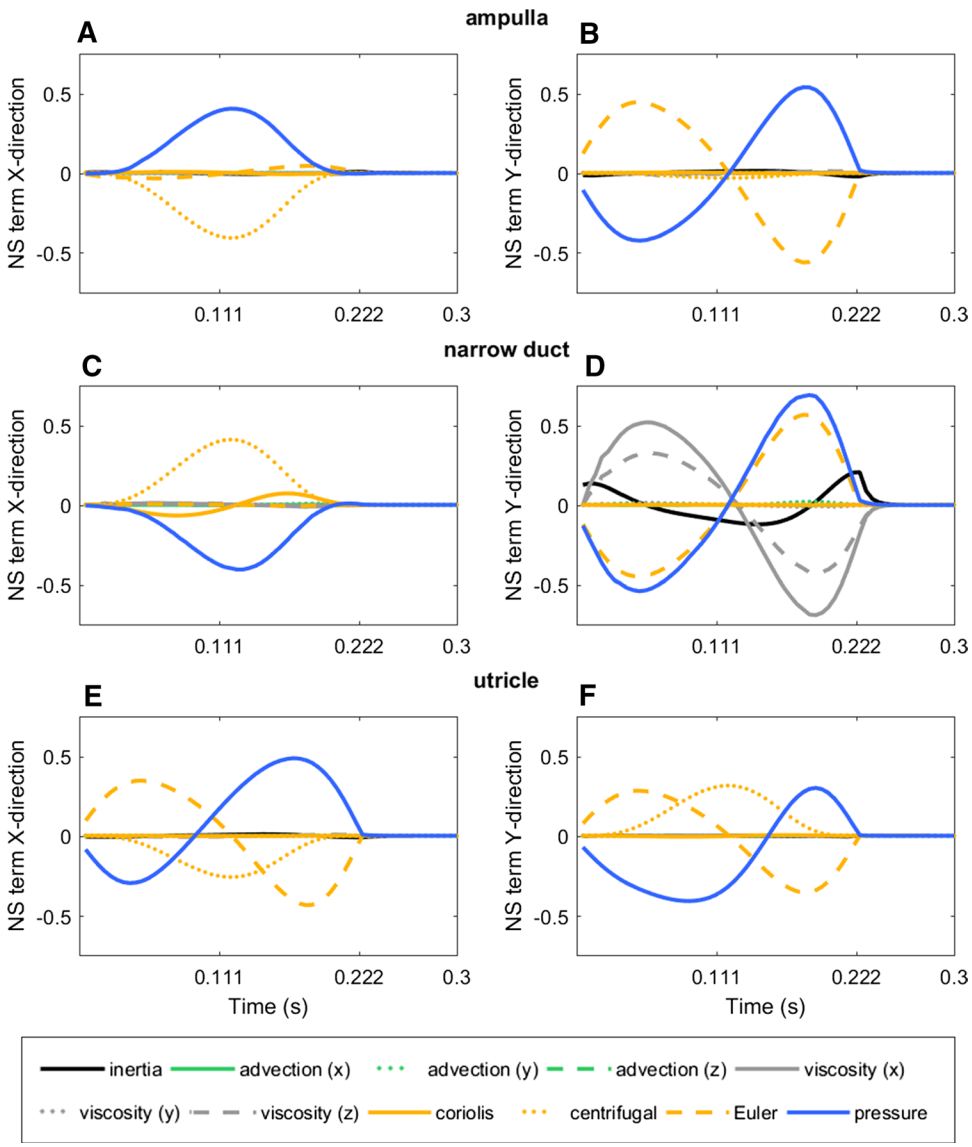

Fig. 7 Navier–Stokes terms in the relative reference frame of model S in *X*-direction (**a**, **c**, **e**) and *Y*-direction (**b**, **d**, **f**). Median values are given for the ampulla (**a**, **b**), narrow duct (**c**, **d**), and utricle (**e**, **f**). For the definition of these zones, see Fig. 2

it), the determining NS terms for model T are the pressure gradient, the centrifugal term, and the Euler term (see Fig. S3), which all have a similar order of magnitude. Due to the spinup/spindown of the model, the magnitude of the Euler term ($\frac{\partial \boldsymbol{\Omega}}{\partial t} \times \boldsymbol{r}$) becomes important, and this is balanced by the pressure gradient. The result is a gradual increase in endolymph pressure from the 'lower' side of the cupula (with negative *Y*-coordinate) to the 'upper' side of the cupula (see Fig. 5e). This causes the pressure difference over the cupula (which, in turn, deforms when it is modelled as a flexible material). In the perpendicular direction (see, e.g. Fig. S3A), the centrifugal term ($\boldsymbol{\Omega} \times (\boldsymbol{\Omega} \times \boldsymbol{r})$) is high. Because the centrifugal force is oriented perpendicular to the force caused by the Euler term, the isobars are skewed, rather than being oriented radially (see Fig. 5e). In the absolute reference frame, the advective and inertial terms balance the pressure gradient, instead of the centrifugal and Euler terms (see Figs. S3 and S4). The importance of the absolute inertial term is caused by the increase in absolute velocity through time, i.e. the velocity in the absolute frame of reference and not relative to the walls of the model (see Fig. 4).

Model H has a human geometry, rather than a simple toroidal shape. Nevertheless, the time profiles of the NS terms are very similar to those of model T, both in the relative and in the absolute frames of reference (see Figs. S5 and S6). In models F and O, the viscous and inertial terms are elevated in the narrow duct due to the fluid flow at this location (see Figs. S7–S10).

In model S, a realistic smooth angular acceleration is imposed on the reference frame, rather than a stepwise ramp function as in model F (see Fig. 3). The resulting time profiles of the NS terms are also smooth, but apart from this shape difference, the patterns are very similar to those of

model F (see relative importance of NS terms in Fig. 7 and S9). In summary, the Euler and centrifugal terms rise due to the spinup of the reference frame, and these terms are balanced by a pressure gradient. The resulting pressure difference over the cupula deforms this flexible sensory structure (see Fig. 5a, b, 6 and S1). In turn, this leads to relative flow in the narrow duct (see Fig. 4b, S1), causing elevated viscous and inertial terms at this location.

4 Discussion

4.1 Effect of the endolymph vortex on cupula displacement

During head rotation, a vortex develops in the utricle which flows in the opposite direction of the imposed acceleration, but only in the relative frame of reference. This vortex is probably caused by fictitious forces (the Euler and centrifugal forces), rather than by turbulence or vortex shedding (see Fig. 7). Hence, the vortex still appears in a (purely hypothetical) inviscid simulation (see Fig. S2). Boselli et al. (2013) were the first to describe this vortex, and they predicted that it may increase cupula displacement and shear strain near the crista of the cupula. In the numeric fluid simulation of Boselli et al. (2013) and in our model with an open ampulla (model O), the vortex causes flow in a clockwise direction in the outer half of the ampulla (near the crista) and flow in an anticlockwise direction in the inner half of the ampulla (see Fig. 4h). In our FSI simulations, the finite element model of the cupula blocks the endolymph flow. However, at the onset of the head manoeuvre, the restorative elastic forces in the cupula are still low. As a result, the velocity profile of the cupula strongly resembles the endolymph velocity profile of a model with an open ampulla (model O, albeit with a lower amplitude), deflecting in clockwise direction at the outer halve of the ampulla (near the crista) and flowing in anticlockwise direction at the inner halve of the ampulla (see Fig. 4h, 6b). This asymmetric, S-shaped cupula displacement increases the deflection of the hair cells that are embedded in the cupula, as suggested by Boselli et al. (2013). For the same maximal cupula displacement, the angular deflection at the crista would be much smaller when the cupula deformed symmetrically. Hence, the asymmetric cupula displacement enhances the sensitivity of the system, and this happens when it is most needed: at the onset (and end) of the head manoeuvre, when the accelerations to be sensed are small.

4.2 Cupula strain

Head rotations are sensed by the vestibular system when sensory hair bundles on the crista surface in the cupula are deflected. The amount of shear strain between the hair bundles in the cupula determines the amount of stimulation of the hair cells in the crista (Rabbitt et al. 2004). We found the highest strain in the cupula is exactly at the location where the hair bundles are embedded. The same was reported by Selva et al. (2009) for a human cupula, based on FEM simulations (without FSI). They found a maximal cupula displacement of 8.5 μm for a pressure difference over the cupula of 0.05 Pa. We found a maximal cupula displacement of 44.2 μm in model S (which is 5.20 times more than Selva). Because the maximal pressure difference in our model (0.27 Pa) is 5.37 times more than simulated by Selva et al., the results can be considered as highly similar. The maximal strain is located at the centre of the crista due to the geometry of the cupula and in particular due to the convex shape of the crista that protrudes into the cupula. The small part of the cupula that attaches to the flanks of the crista, can hardly deflect under the imposed fluid pressure. It is mainly the rest of the cupula, which extends from the top of the crista to the roof of the ampulla, that deforms during the head manoeuvre (see Fig. 6d). As this main body of the cupula stretches over the top of the crista, strain accumulates at this location.

The location with the highest strain (the central part of the crista) is also the zone with the most sensitive neural afferents (Eatock and Songer 2011). These irregularly spiking afferents are most probably specialized in fast and reliable signal transmission (Goldberg and Fernández 1977; Goldberg 2000). They are also more sensitive to velocity changes than the regularly spiking afferents from the periphery of the crista (Goldberg 2000). Together, the geometry of the crista, the discussed flow patterns, and the transmission characteristics of the afferents in the central zone seem optimally adapted for sensing short and small cupula displacements and make the vestibular system very sensitive to even the finest head manoeuvres.

4.3 Time scales and cupula overshoot

The calculated short and long time scales in the most realistic model (i.e. in model S; time scales of, respectively, 0.014 s and 3.33 s) agree with values reported in the literature based on both models and experiments (Muller 1990; Dai et al. 1999; Obrist 2011). The long time scale reflects the time required for the cupula to return from its overshot deformed state to its relaxed state after the end of the head manoeuvre. The overshoot occurs because the cupula already starts relaxing during the head manoeuvre. Combined with its backward movement during head deceleration, this causes the cupula to overshoot its relaxed position (Obrist et al. 2010). Since the long time scale is in the order of a couple of seconds, it is logical that the

overshoot is very small and occurs only at the very end of the short alarm turn head manoeuvre.

4.4 Vestibular system mechanics interpreted in the relative reference frame

The vestibular system senses head manoeuvres because, when the endolymph fluid lags behind due to inertia, endolymph flow deforms the cupula (Kandel et al. 1991; Muller and Verhagen 2002; Rabbitt et al. 2004, 2009; Angelaki and Cullen 2008; Latash 2008; Ekdale 2016; Grohé et al. 2016; Djukic and Filipovic 2017). This is a reasoning in the *absolute* frame of reference. The cupulas are attached to vestibular system walls, and, therefore, they are attached to a *relative* (co-rotating) frame of reference. The pressure distribution, which causes the cupula to deflect, is the same in both the relative and the absolute frame of reference. However, the NS equations show that the interpretation of the mechanical cause of the pressure distribution depends on the reference frame that is taken into consideration. In the absolute frame of reference, it is the inertial term (related to the high *absolute* endolymph flow velocity) that balances the pressure distribution in Y-direction in the ampulla (see Fig. S11B). In the relative frame of reference, on the other hand, the endolymph velocity stays very low in the ampulla (see Fig. 4b). Here, it is the Euler term, rather than the inertial term, that balances the pressure distribution in *Y*-direction (see Fig. 7b). Since the Euler term does not depend on the flow velocity relative to the (rotating) labyrinth wall, no high *relative* endolymph flow is necessary for the cupula to deflect.

4.5 Usefulness of simplified models

Given the technical challenge of creating a fluid–structure interaction model, it is worth questioning when it is really necessary to construct such a detailed simulation model. Obviously, only an FSI model provides the detailed strain distribution in the cupula in response to the endolymph dynamics. However, we also found that simplified models, with a stylized geometry and/or a rigid cupula yield very similar NS terms and endolymph flow as more realistic models with a deformable cupula and smooth velocity profile.

Acknowledgements This research was financially supported by FWO Project G0E02.14N to prof. Peter Aerts, FWO postdoctoral fellowship 12R5118N to J.G. and FWO travel Grant V428716N to J.G. for a long stay abroad at the Laboratory for Aero and Hydrodynamics at the TUDelft. Simulation software licences and computers were funded by FWO research Grant 1504018N to J.G and by Grant BOF/KP 24346 of University of Antwerp to prof. Peter Aerts. The authors wish to thank Dr. Sam Van Wassenbergh for advice on the construction of the simulation model, Ms. Josie Meaney-Ward for language correction, and two anonymous referees for their valuable comments and remarks.

Compliance with ethical standards

Conflict of interest The authors declare that they have no conflict of interest.

References

Angelaki DE, Cullen KE (2008) Vestibular system: the many facets of a multimodal sense. Annu Rev Neurosci 31:125–150. https://doi.org/10.1146/annurev.neuro.31.060407.125555

Batchelor GK (2007) An introduction to fluid dynamics. Cambridge University Press, Cambridge

Berg T (2011) Solution stabilization for FSI and 6DOF with fluent. Ansys Inc. Report and Tutorial

Boselli F, Obrist D, Kleiser L (2013) Vortical flow in the utricle and the ampulla: a computational study on the fluid dynamics of the vestibular system. Biomech Model Mechanobiol 12:335–348. https://doi.org/10.1007/s10237-012-0402-y

Boselli F, Kleiser L, Bockisch CJ et al (2014) Quantitative analysis of benign paroxysmal positional vertigo fatigue under canalithiasis conditions. J Biomech 47:1853–1860. https://doi.org/10.1016/j.jbiomech.2014.03.019

Cullen KE (2012) The vestibular system: multimodal integration and encoding of self-motion for motor control. Trends Neurosci 35:185–196. https://doi.org/10.1016/j.tins.2011.12.001

Curthoys IS, Oman CM (1987) Dimensions of the horizontal semicircular duct, ampulla and utricle in the human. Acta Otolaryngol 103:254–261

Dai M, Klein A, Cohen B, Raphan T (1999) Model-based study of the human cupular time constant. J Vestib Res 9:293–301

Djukic T, Filipovic N (2017) Numerical modeling of the cupular displacement and motion of otoconia particles in a semicircular canal. Biomech Model Mechanobiol 16:1669–1680. https://doi.org/10.1007/s10237-017-0912-8

Eatock RA, Songer JE (2011) Vestibular hair cells and afferents: two channels for head motion signals. Ann Rev Neurosci 34:501–534. https://doi.org/10.1146/annurev-neuro-061010-113710

Ekdale EG (2016) Form and function of the mammalian inner ear. J Anat 228:324–337. https://doi.org/10.1111/joa.12308

Goldberg JM (2000) Afferent diversity and the organization of central vestibular pathways. Exp Brain Res 130:277–297. https://doi.org/10.1007/s002210050033

Goldberg JM, Fernández C (1977) Conduction times and background discharge of vestibular afferents. Brain Res 122:545–550

Grieser B, Obrist D, Kleiser L (2013) Validation of assumptions on the endolymph motion inside the semicircular canals of the inner ear. Internal Reports of the Institute of Fluid Dynamics, ETH Zurich. https://doi.org/10.3929/ethz-a-007588055

Grieser BJ, Kleiser L, Obrist D (2016) Identifying mechanisms behind the Tullio phenomenon: a computational study based on first principles. J Assoc Res Otolaryngol 17:103–118. https://doi.org/10.1007/s10162-016-0553-0

Grohé C, Tseng ZJ, Lebrun R et al (2016) Bony labyrinth shape variation in extant Carnivora: a case study of Musteloidea. J Anat 228:366–383. https://doi.org/10.1111/joa.12421

Kandel ER, Schwartz JH, Jessell TM (1991) Principles of neural science, 3rd edn. International edition. Prentice-Hall International Inc., New Jersey, p 1135. ISBN 0-83858068-8

Kassemi M, Deserranno D, Oas JG (2005) Fluid–structural interactions in the inner ear. Comput Struct 83:181–189. https://doi.org/10.1016/j.compstruc.2004.08.001

Latash ML (2008) Neurophysiological basis of movement, 2nd edn. Human Kinetics, Champaign

Lorente de Nó R (1927) Contribucion al estudio matematico del organo del equilibrio. Trab Publ En La 7:202–206

McLaren JW, Hillman DE (1979) Displacement of the semicircular canal cupula during sinusoidal rotation. Neuroscience 4:2001–2008

Muller M (1990) Relationships between semicircular duct radii with some implications for time constants. Neth J Zool 40:173–202

Muller M, Verhagen JHG (1988) A new quantitative model of total endolymp flow in the system of semicircular ducts. J Theor Biol 134:473–501

Muller M, Verhagen JHG (2002) Optimization of the mechanical performance of a two-duct semicircular duct system part 1: dynamics and duct dimensions. J Theor Biol 216:409–424. https://doi.org/10.1006/yjtbi.3003

Njeugna E, Eichhorn JL, Kopp C, Harlicot P (1992) Mechanics of the cupula: effects of its thickness. J Vestib Res Equilib Orientat 2:227–234

Obrist D (2008) Fluidmechanics of semicircular canals—revisited. Z Angew Math Phys 59:475–497. https://doi.org/10.1007/s00033-007-6037-7

Obrist D (2011) Fluid mechanics of the inner ear. Habilitation treatise in Fluid Mechanics at ETH Zurich. p 182. https://doi.org/10.3929/ethz-a-007318979

Obrist D, Hegemann S, Kronenberg D et al (2010) In vitro model of a semicircular canal: design and validation of the model and its use for the study of canalithiasis. J Biomech 43:1208–1214. https://doi.org/10.1016/j.jbiomech.2009.11.027

Oman CM, Marcus EN, Curthoys IS (1987) The influence of semicircular canal morphology on endolymph flow dynamics. An anatomically descriptive mathematical model. Acta Otolaryngol 103:1–13. https://doi.org/10.3109/00016488709134691

Rabbitt RD (1999) Directional coding of three-dimensional movements by the vestibular semicircular canals. Biol Cybern 80:417–431. https://doi.org/10.1007/s004220050536

Rabbitt RD, Boyle R, Highstein SM (1995) Mechanical indentation of the vestibular labyrinth and its relationship to head rotation in the toadfish, Opsanus tau. J Neurophysiol 73:2237–2260

Rabbitt RD, Damiano ER, Grant WJ (2004) Biomechanics of the semicircular canals and otolith organs. In: Highstein SM, Fay RR (eds) The vestibular system. Springer, New York, pp 153–201

Rabbitt RD, Breneman KD, King C et al (2009) Dynamic displacement of normal and detached semicircular canal cupula. JARO—J Assoc Res Otolaryngol 10:497–509. https://doi.org/10.1007/s10162-009-0174-y

Santos CF, Belinha J, Gentil F et al (2017a) Biomechanical study of the vestibular system of the inner ear using a numerical method. Procedia IUTAM 24:30–37. https://doi.org/10.1016/J.PIUTAM.2017.08.040

Santos CF, Belinha J, Gentil F et al (2017b) An alternative 3D numerical method to study the biomechanical behaviour of the human inner ear semicircular canal. Acta Bioeng Biomech 19:3–15. https://doi.org/10.5277/ABB-00498-2015-03

Selva P, Oman CM, Stone HA (2009) Mechanical properties and motion of the cupula of the human semicircular canal. J Vestib Res Equilib Orientat 19:95–110. https://doi.org/10.3233/VES-2009-0359

Squire LR, Berg D, Bloom FE (2013) Fundamental neuroscience. Elsevier/Academic Press, Amsterdam

Steer RW, Li, Yao T, Young LR, Meiry JL (1967) Physical properties of the labyrinthine fluids and quantification of the phenomenonof caloric stimulation. In: 3rd Symposium on the role of the vestibular organs in space exploration, pp 409–420

Steinhausen W (1933) Über die beobachtung de cupula in den bogengangsam pullen des labyrinths des lebenden hechts. Pflugers Arch Gesamte Physiol Menschen Tiere 232:500–512

Van Buskirk WC, Watts RG, Liu YK (1976) The fluid mechanics of the semicircular canals. J Fluid Mech 78:87–98. https://doi.org/10.1017/S0022112076002346

Wu C, Hua C, Yang L et al (2011) Dynamic analysis of fluid–structure interaction of endolymph and cupula in the lateral semicircular canal of inner ear. J Hydrodyn Ser B 23:777–783. https://doi.org/10.1016/S1001-6058(10)60176-X

Yamauchi A, Rabbitt RD, Boyle R, Highstein SM (2002) Relationship between inner-ear fluid pressure and semicircular canal afferent nerve discharge. J Assoc Res Otolaryngol 3:26–44. https://doi.org/10.1007/s101620010088